



LAWRENCE  
LIVERMORE  
NATIONAL  
LABORATORY

# Dilepton Tagged Jets in Heavy-Ion Collisions at the LHC

C. Mironov, M. Castro, P. Constantin, G. J.  
Kunde, R. Vogt

September 18, 2010

Journal of Physics G

## **Disclaimer**

---

This document was prepared as an account of work sponsored by an agency of the United States government. Neither the United States government nor Lawrence Livermore National Security, LLC, nor any of their employees makes any warranty, expressed or implied, or assumes any legal liability or responsibility for the accuracy, completeness, or usefulness of any information, apparatus, product, or process disclosed, or represents that its use would not infringe privately owned rights. Reference herein to any specific commercial product, process, or service by trade name, trademark, manufacturer, or otherwise does not necessarily constitute or imply its endorsement, recommendation, or favoring by the United States government or Lawrence Livermore National Security, LLC. The views and opinions of authors expressed herein do not necessarily state or reflect those of the United States government or Lawrence Livermore National Security, LLC, and shall not be used for advertising or product endorsement purposes.

# Dilepton Tagged Jets in Heavy-Ion Collisions at the LHC

C. Mironov, M. Castro, P. Constantin, G. J. Kunde

E-mail: [camelia.mironov@cern.ch](mailto:camelia.mironov@cern.ch)  
Los Alamos National Laboratory

Ramona Vogt

E-mail: [vogt@lbl.gov](mailto:vogt@lbl.gov)  
Lawrence Livermore National Laboratory and UC Davis

**Abstract.** The properties of the new state of matter created at RHIC will be further investigated at the LHC. High transverse momentum jets will play a key role in these studies. While traversing the medium, the hard partons that fragment into jets will lose energy through collisions and radiation, modifying the jet properties. By measuring in-medium modifications of jets, we gain information about the medium itself. Here we discuss decays of high transverse momentum  $\gamma^*$  and  $Z^0$  to lepton pairs in association with quark or gluon jets. Semileptonic  $B\bar{B}$  and  $D\bar{D}$  decays to dileptons, the main background, is investigated at next-to-leading order using **HVQMNR**, an exclusive next-to-leading order  $Q\bar{Q}$  calculation.

Submitted to: *J. Phys. G: Nucl. Phys.*

## 1. Introduction

A new state of matter is believed to have been created in  $\sqrt{s_{NN}} = 200$  GeV relativistic heavy-ion collisions at RHIC [1]. The challenge for the LHC heavy-ion program is to study the properties (*e.g.* temperature and energy density) of this new form of matter. A powerful tool for this purpose, developed at RHIC [2], is the study of dijets via leading hadron correlations. In particular, dihadron *angular* and *transverse momentum* correlations study back-to-back hard scattered partons that propagate in the medium before fragmenting into hadron jets [3]. While traversing the medium, the partons lose energy through collisions and radiation. The shape of the  $p_T$  and angular distributions of the final hadrons, obtained from parton fragmentation, will also be modified. Through differential measurements of these in-medium modifications, we infer the properties of the medium via theoretical models. For example, pQCD-based models [4] of parton energy loss in a dense, colored medium can be employed to determine the gluon rapidity density as a function of time using a model for the collision geometry and for the radial

and the longitudinal expansion dynamics. This gluon density can be related to the temperature of the plasma via the number of gluon degrees of freedom.

Such correlation studies are also essential in elementary  $pp$  collisions to determine the baseline reference. Medium modifications in heavy-ion collisions can only be interpreted relative to this baseline.

In this paper, we investigate a jet channel which is energetically possible for the first time at heavy-ion colliders: decays of high transverse momentum,  $p_T$ , virtual photons ( $\gamma^*$ ) and  $Z^0$  bosons in association with hadron jets [5, 6]. The production channels we study are  $q + \bar{q} \rightarrow \gamma^*/Z^0 + g$  (annihilation) and  $g + q \rightarrow \gamma^*/Z^0 + q$  (Compton scattering) with the subsequent dilepton decay of the vector boson,  $\gamma^*/Z^0 \rightarrow l^-l^+$  ( $l = e, \mu$ ), and fragmentation of the parton,  $q/g \rightarrow \text{jet}$ . Because leptons interact weakly with the medium, their reconstructed momentum provides direct access to the initial momentum of the opposite-side jet, making the jet analyses more accurate.

Though this analysis should be performed in both azimuth (in the plane perpendicular to the beam axis) and rapidity (along the beam axis), we only discuss the azimuthal analysis here. We do not discuss detector reconstruction performance in detail and consider only muons within the CMS and ATLAS detector acceptances:  $p_T^\mu > 3.5 \text{ GeV}/c$  and  $|\eta^\mu| < 2.4$ . Since the branching ratios to electrons and muons for the signal decays are the same, scaling these rates to electrons from muons should be straightforward. The statement is valid also for the background decays. However, while we are confident that electrons can also be used to both increase the signal and study the background, analyses of the electron detection capabilities of the electromagnetic calorimeters, beyond the scope of this work, must be made.

The paper is structured as follows. Section 2 presents a case study for the extraction of the parton fragmentation distribution using the angular and momentum correlation method. In Sec. 3, we focus on the  $Z^0/\gamma^*$ +jet signal rates. Sections 4 and 5 discuss the dimuon background sources and rejection methods. Section 6 contains the conclusions of this paper.

## 2. Jet studies using opposite-sign dileptons with momentum and angular correlations

Jets are a proven high  $Q^2$  QCD probe of hard production and fragmentation. There are basically two complementary methods for identifying jets and measuring their properties. The first is an event-by-event method (where event means a collision registered by a detector) which uses a model/algorithm (cone,  $k_T$  etc.) together with calorimetric information to reconstruct the total jet energy. This algorithmic method was successfully used at the Tevatron and the ISR in  $p\bar{p}$  and  $pp$  collisions respectively. It has also recently been applied to heavy-ion collisions at RHIC [7]. Unfortunately, the jet reconstruction efficiency and the ability to discriminate jets over the hadronic background decreases with decreasing jet momentum and with increasing detector occupancy. The occupancy can be rather large in high-multiplicity heavy-ion

collisions or high-energy, high-luminosity  $pp$  collisions. The second method, employing momentum and angular correlations, complements the first since it accesses the entire jet  $p_T$  spectrum. In addition, low  $p_T$  studies are desirable since these jets are more likely to display large medium effects. Also, the background can be relatively easily accounted for within this method, independent of the collision density. The principles of this statistical method are presented in the following, using the  $Z^0$ +jet channel for illustration (Fig. 1).

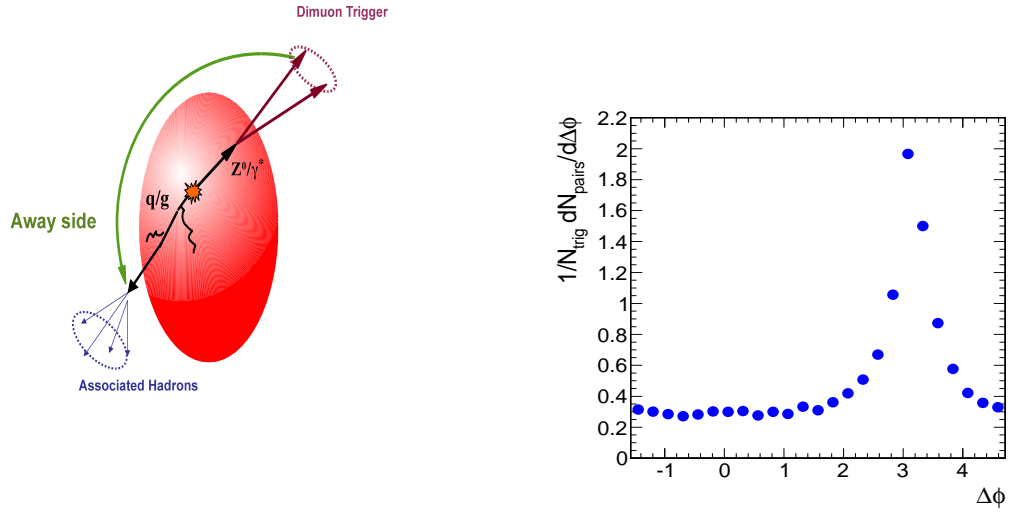


**Figure 1.** Left: Cartoon illustrating the  $(Z^0/\gamma^* \rightarrow \mu\mu)$ +jet geometry. Right: Relative azimuthal angle between the trigger dimuon and the associated charged hadron.

On an event-by-event basis, *trigger* dimuons from  $Z^0/\gamma^*$  decays are identified and paired with all *associated* hadrons in the same event but within different transverse momentum intervals. The azimuthal distribution per trigger particle (Fig. 1, right) is defined as

$$Y(\Delta\phi) = \frac{\sum_{\text{evt}} N_{\text{pairs}}(\Delta\phi)}{\sum_{\text{evt}} N_{\text{trig}}} \quad (1)$$

where  $\Delta\phi = \phi^{\text{trig}} - \phi^{\text{assoc}}$ ,  $N_{\text{pairs}}(\Delta\phi)$  are the trigger-associated pairs falling in the  $\Delta\phi$  interval and  $N_{\text{trig}}$  are all triggers, both summed over all events. The shape of this distribution is that expected for a  $X$ +jet channel, in which the  $X$  is a trigger that does not interact strongly with the medium (*e.g.*  $\gamma$  or dimuons from  $Z^0/\gamma^*$  decays): there are no correlations on the same side of the trigger (no peak around  $\Delta\phi \sim 0$ ), but only on the away side (around  $\Delta\phi \sim \pi$ ), from correlations with hadrons from the fragmentation of the away-side parton ( $q$  or  $g$ ).

Next,  $Y(\Delta\phi)$  distributions are generated for a fixed dimuon trigger transverse momentum,  $p_T^{\text{trig}}$ , interval and several transverse momentum intervals for associated

hadrons,  $p_T^{\text{assoc}}$ , intervals. After extracting the away-side,  $\Delta\phi \sim \pi$ , jet component, the dependence of the away-side yield,  $Y(\Delta\phi \sim \pi)$ , in a fixed  $p_T^{\text{trig}}$  interval as a function of  $z = p_T^{\text{assoc}}/p_T^{\text{trig}}$  can be used to construct a fragmentation distribution:

$$D(z) = \frac{1}{N_{\text{trig}}} \frac{dY(\Delta\phi \sim \pi)}{dz} \Big|_{p_T^{\text{trig}} \text{ fixed}}. \quad (2)$$

Since  $D(z)$  contains all hadronic fragments of the initial parton, including those arising from medium-induced gluon radiation off the parton, it is not the vacuum fragmentation function measured in  $e^+e^-$  collisions even though this terminology is typically used in the literature. Thus, measuring these  $D(z)$  distributions in both  $pp$  and Pb+Pb collisions, we will be able to infer the in-medium modifications to the fundamental QCD fragmentation.

Another possible measurement with fundamental impact on the understanding of the medium properties involves the width of the  $\Delta\phi$  distributions of the away jet. As detailed in Appendix A, the  $\Delta\phi$  distributions reflect the contributions from three main sources: the initial parton transverse momentum,  $k_T$ ; the transverse momentum accrued during fragmentation,  $j_T$ ; and multiple scattering (initial and final-state radiation). Hence, by measuring the width of the  $\Delta\phi$  distributions in different combinations of  $p_T^{\text{trig}}$  and  $p_T^{\text{assoc}}$ , it is possible to directly access the different parton transverse momentum sources.

The channel we focus on in this study,  $Z^0/\gamma^* + \text{jet}$ , has several advantages over other similar analyses. In traditional dijet analyses in heavy-ion collisions [1] where the trigger is the leading hadron of one jet, correlations generated by the elliptic flow,  $v_2$ , of single hadrons with respect to the reaction plane [8] have to be subtracted. Because, to first order, the leptons couple weakly to the medium, this type of collective background is not important for lepton-tagged jets.

In addition, in dijet analyses, both jets may be affected by the medium. Thus the *initial* jet energy can be unknown, giving large uncertainties on the initial parton energy. To resolve the problem, Wang and collaborators [9, 10] suggested studying the  $z = p_T^{\text{hadron}}/p_T^{\gamma}$  distribution in  $\gamma + \text{jet}$  processes. Measurement of the initial jet  $p_T$  is possible since  $\vec{p}_T^{\text{parton}} \approx -\vec{p}_T^{\gamma}$  when the hadronic probe on one side is replaced by an electromagnetic probe. The photon couples weakly with the medium and conserves its initial kinematics while the parton energy is attenuated. The relation is valid modulo intrinsic parton transverse momentum,  $k_T$ , effects (finite size of the nucleons, initial-state radiation). The jet is thus tagged by the photon, *i.e.* a  $\gamma$ -tag. There are several difficulties with this measurement, primarily arising from misidentification of the background and signal. A direct photon cluster can combine in the calorimeter with a  $\pi^0$  decay cluster and will be rejected if the resulting cluster has the invariant mass of a  $\pi^0$ . If a  $\pi^0$  decay gamma is lost either due to detector inefficiency or acceptance cuts, the remaining decay photon can be misidentified as a real direct photon. At high  $p_T$ , two-photon clusters from  $\pi^0$  decays can merge, leaving a single cluster in the calorimeter, faking a direct photon signal. Photons produced by collinear fragmentation of a hard quark or gluon [11] can also be misidentified as direct photons.

Dilepton+jet studies enjoy the same advantages of  $\gamma$ +jet probes but with fewer drawbacks. The dilepton+jet measurement overcomes the obstacles of the  $\gamma$ +jet analysis while retaining the characteristics of a ‘golden channel’. The only drawback is the significantly lower cross section relative to the  $\gamma$ +jet yield, see Fig. 2. However, due to the technical considerations mentioned in the previous paragraph, in heavy-ion collisions at the LHC, the  $\gamma$  measurement in the  $\gamma$ +jet channel is robust only above  $p_T^\gamma \sim 80 - 100 \text{ GeV}/c$  in CMS [12] and ATLAS [13]. With this  $p_T$  limitation, the  $\gamma$ +jet rate is comparable to the  $Z^0$ +jet rate for  $p_T^{Z^0} > 25 \text{ GeV}/c$ , as we discuss in the next section. Hence, the dilepton-tagged channel complements the photon-tagged channel by making lower  $p_T$  jets accessible.

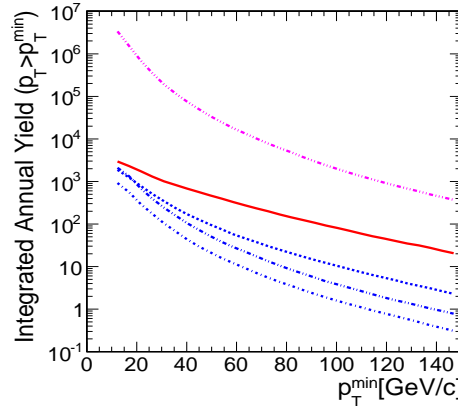


**Figure 2.** Integrated annual yield of tagged jets in Pb+Pb collisions at  $\sqrt{s_{NN}} = 5.5 \text{ TeV}$  with  $0.5 \text{ nb}^{-1}$  integrated luminosity, as a function of the integration lower bound  $p_T^{\min}$  of the trigger ( $\gamma$  or dimuons from  $\gamma^*/Z^0$  decays). From top to bottom the curves show  $\gamma$  tags (dotted line) compared to dimuon tags from  $Z^0$  (continuous line) and  $\gamma^*$  decays in several invariant mass intervals:  $M > 12 \text{ GeV}/c^2$  (dashed line),  $4.0 < M < 8.5 \text{ GeV}/c^2$  (dot-dot-dashed line) and  $1.3 < M < 2.7 \text{ GeV}/c^2$  (dot-dashed line).

### 3. The $Z^0/\gamma^*$ +jet signal

We consider Pb+Pb collisions at  $\sqrt{s_{NN}} = 5.5 \text{ TeV}$  with an instantaneous luminosity of  $L = 5 \times 10^{26} \text{ cm}^{-2}\text{s}^{-1}$ , the average value for the first year heavy-ion run at the LHC. Assuming a  $10^6 \text{ s}$  run, corresponding to one month of collisions at 50% efficiency leads to an integrated luminosity of  $0.5 \text{ nb}^{-1}$ . The unmodified rates for Pb+Pb collisions are obtained by scaling from  $pp$  collisions at the same energy assuming  $\sigma_{AA} = A^2 \sigma_{pp}$ . In this paper, the trigger (trig) refers to a muon pair from  $Z^0/\gamma^*$  or  $Q\bar{Q}$  decays while the associated away-side jet (assoc) always comes from the accompanying light parton unless otherwise specified.

**Table 1.** The integrated annual yield of dimuon triggers from  $Z^0$  and  $\gamma^*$  decays for different invariant mass intervals in Pb+Pb collisions at  $\sqrt{s_{NN}} = 5.5$  TeV and  $L = 0.5 \text{ nb}^{-1}$  with four different values of  $p_T^{\text{min}}$ .

Signal/Trigger	$p_T^{\text{min}}(\text{GeV}/c)$			
	10	20	30	50
$Z^0$	3000	1800	900	500
$\gamma^*$ ( $M > 12 \text{ GeV}/c^2$ )	1900	750	300	90
$\gamma^*$ ( $4.0 < M < 8.5 \text{ GeV}/c^2$ )	2100	750	200	40
$\gamma^*$ ( $1.3 < M < 2.7 \text{ GeV}/c^2$ )	900	300	100	20

### 3.1. Rates and yields

The  $Z^0/\gamma^*$ +jet rates in  $pp$  collisions were obtained using PYTHIA 6.32 [14] with default parameters and the CTEQ5M PDFs. To generate sufficient statistics, several PYTHIA switches were used. We first turned off all PYTHIA processes (MSEL=0) and then selected  $q + \bar{q} \rightarrow Z^0/\gamma^* + g$  (ISUB=15) and  $q + g \rightarrow Z^0/\gamma^* + q$  (ISUB=30), separating the  $Z^0$  (MSTP(43)=2) from the  $\gamma^*$  (MSTP(43)=1) contributions. To obtain good statistics at high transverse momentum, we simulated 10K events in 10 GeV wide  $\hat{p}_{T\ddagger}$  bins between 10 and 300 GeV/ $c$ . We selected only *dimuon* decays which had single muons with  $p_T > 3.5 \text{ GeV}/c$  and  $|\eta| < 2.4$ , to fall within the CMS and ATLAS acceptances. The final signal spectrum was obtained by scaling each bin by the corresponding cross section,  $(\sigma(\hat{p}_T))$ , and summing over all bins.

The PYTHIA signal simulations at  $\sqrt{s_{NN}} = 5.5 \text{ TeV}$  are presented in Fig. 2. The integrated yield above a given minimum trigger  $p_T$  is shown for  $Z^0$ +jet and  $\gamma^*$ +jet (in three different mass intervals) events and, for comparison,  $\gamma$ +jet events. The highest dimuon mass interval,  $M > 12 \text{ GeV}/c^2$ , is the PYTHIA default. To increase the dimuon statistics for the  $\gamma^*$ -tagged jets, we looked at lower mass windows:  $M_\eta, M_\phi < M < M_{J/\psi}$  ( $1.3 < M < 2.7 \text{ GeV}/c^2$ ) and  $M_{\psi'} < M < M_\Upsilon$  ( $4 < M < 8.5 \text{ GeV}/c^2$ ).

Table 1 gives the integrated dimuon+jet yields for four values of  $p_T^{\text{min}}$  in Fig. 2. At lower dimuon  $p_T$ , the summed  $\gamma^*$ +jet contributions are greater than 50% for  $p_T^{\text{min}} < 30 \text{ GeV}/c$  relative to the  $Z^0$  signal. Hence, if the contributions from these channels can be extracted from the background, the overall dilepton-tagged jet signal rate will increase significantly.

The minimum dimuon momentum is directly related to the physics we want to address with the dilepton-hadron angular correlation analysis. The initial assumption,  $p_T^{\mu\mu} \approx p_T^{\text{jet}}$ , necessary for a precise measurement of the fragmentation distribution of the jet, is valid for  $p_T^{\text{jet}} \gg k_T$ , the intrinsic parton transverse momentum. Previous studies [15] showed that  $k_T$  effects are more important at lower  $p_T$ , *e.g.* below  $\approx 30 \text{ GeV}/c$  for direct photon production at Tevatron.

The choice of the lower limit on  $p_T$  is also driven by the charged-track reconstruction capabilities of the detectors which impacts the associated hadron reconstruction. Considering that  $\approx 20\%$  of the initial parton  $p_T$  is carried by the leading hadron, a

‡ Here  $\hat{p}_T$  is the  $p_T$  of the outgoing parton/ $Z^0$  in the center of mass of the hard scattering.



parton with  $p_T = 25 \text{ GeV}/c$  will produce a leading hadron with  $\langle p_T \rangle \sim 5 \text{ GeV}/c$ . Thus a lower limit of  $25 \text{ GeV}/c$  on the  $p_T^{\text{trig}}$  cut ensures that most of the jet fragments have a transverse momentum bigger than  $1 \text{ GeV}/c$ , a region in which both the CMS [16] and ATLAS [17] trackers perform well in terms of efficiency and purity of the reconstructed tracks.

Furthermore, we find that the shape of the  $z$  distribution is independent of  $k_T$  for  $p_T^{\text{trig}} > 25 \text{ GeV}/c$  by varying  $\sqrt{\langle k_T^2 \rangle}$  between 0 and  $5 \text{ GeV}/c$ . In Appendix A we also discuss the contributions to the  $\Delta\phi$  distributions in  $pp$  collisions, the baseline measurement. Since ultimately the goal is to study the medium created in heavy-ion collisions starting from the modifications of the  $\Delta\phi$  distributions, it is important to insure that some of the contributions to these distributions from non-medium effects are negligible.

## 4. Background

A successful dilepton-tag jet measurement, as we propose (using the angular-correlation method), requires a clean identification of the tag, the dimuon signal. We will focus in the following on the dominant background for the opposite-sign dimuon signal, the semileptonic  $D\bar{D}$  and  $B\bar{B}$  decays, and briefly mention another, dijets from light partons.

**Table 2.** The input parameters for HVQMNR:  $\langle k_T \rangle$  is the mean intrinsic transverse momentum;  $\epsilon$  is the Peterson function fragmentation parameter; and  $\mu_F/m_T$  and  $\mu_R/m_T$  are ratios of the factorization and renormalization scales to the heavy quark transverse mass,  $m_T = \sqrt{p_T^2 + m^2}$ , where  $m$  is the heavy quark mass and  $p_T$  is that of the  $Q\bar{Q}$  pair. The CTEQ6M parton densities are used in the calculations.

$Q$	$m \text{ (GeV}/c^2\text{)}$	$\langle k_T \rangle \text{ (GeV}/c\text{)}$	$\epsilon$	$\mu_F/m_T$	$\mu_R/m_T$
$c$	1.5	1.0	0.06	1.0	1.0
$b$	4.75	1.0	0.006	1.0	1.0

### 4.1. Muons from heavy mesons

The decay chain  $D\bar{D}/B\bar{B} \rightarrow \mu\mu + X$  produces a muon pair similar to the dimuon signal from  $Z^0/\gamma^*$  decays. Previous studies were performed for the LHC [18, 19] using the HVQMNR [20] code which calculates exclusive heavy quark production at next-to-leading-order (NLO). The azimuthal distributions of dimuons from  $Q\bar{Q}$  pair decays are relatively isotropic when no cuts are applied. This is not unexpected since the  $Q\bar{Q}$  pairs are produced back-to-back only at leading order while at NLO the pairs are often accompanied by a third hard parton (jet), randomizing the azimuthal distributions [19].

We present here a detailed study of the kinematics of heavy quark production and the subsequent decay dimuons. The input HVQMNR parameters are given in Table 2. The mean intrinsic parton transverse momentum,  $\langle k_T \rangle$ , smears the  $Q\bar{Q}$  pair distributions in  $p_T$  and  $\Delta\phi$ . The hadronization process employs the Peterson fragmentation function [21],  $D(z) = N/[z(1 - 1/z - \epsilon/(1 - z))^2]$ , where  $\epsilon$  approximates

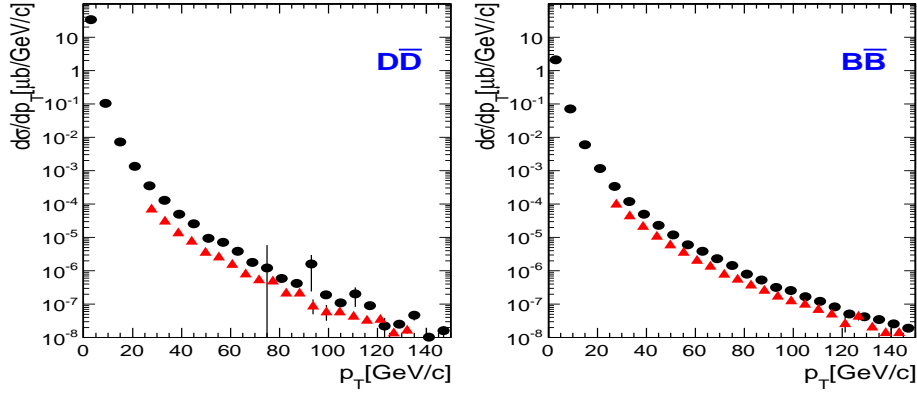


**Figure 3.** The dimuon  $p_T$  distributions for  $D\bar{D}$  (left) and  $B\bar{B}$  (right) decays. The circles show the distributions with no kinematic cuts while the triangles are dimuons filtered through the CMS/ATLAS acceptance.

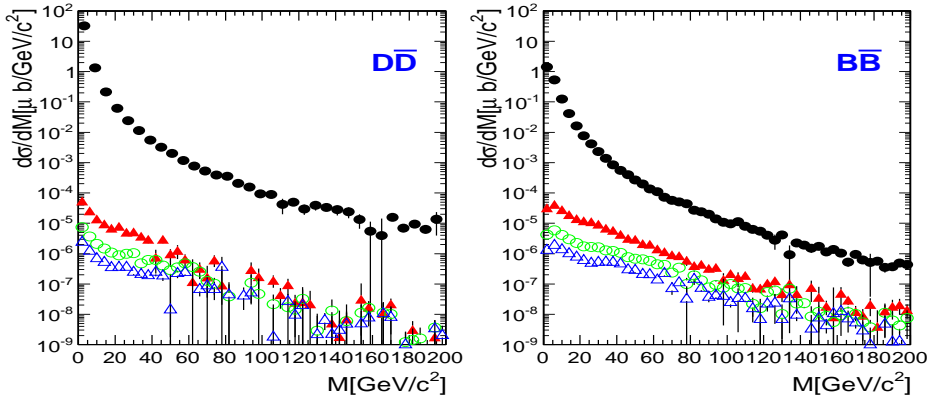


**Figure 4.** The dimuon mass distributions from  $D\bar{D}$  (left) and  $B\bar{B}$  (right) decays. The filled circles do not include any cuts. The other symbols show simulations with CMS/ATLAS-appropriate cuts on the single muons as well as an increasing dimuon  $p_T$  cut: filled triangles,  $p_T > 25$  GeV/c; open circles,  $p_T > 40$  GeV/c; open triangles,  $p_T > 50$  GeV/c.

the ratio of the light to heavy quark masses. The ratios  $\mu_F/m_T$  and  $\mu_R/m_T$  are the ratios of the factorization and renormalization scales to the transverse mass of the  $Q\bar{Q}$  pair,  $m_T = \sqrt{m^2 + \langle p_T^2 \rangle}$ , where  $m$  is the heavy quark mass and  $\langle p_T^2 \rangle$  is the average of the quark and antiquark transverse momenta. We use the CTEQ6M parton distribution functions [22]. The generic branching ratios for heavy flavor decays to leptons are  $\mathcal{B}(D \rightarrow \mu X) = 10.3\%$  and  $\mathcal{B}(B \rightarrow \mu X) = 10.86\%$  [23].

The azimuthal angle, pair mass and transverse momentum distributions with and without muon cuts are presented in more detail in Appendix C. Here we present the dimuon  $p_T$  and invariant mass,  $M$ , distributions and show the influence of a minimum dimuon  $p_T$  cut on the rates. *Detector cuts*,  $p_T^\mu > 3.5$  GeV/c and  $|\eta^\mu| < 2.4$ , are imposed on single muons.

Figure 3 shows the  $p_T$  distributions for dimuons from  $D\bar{D}$  (left) and  $B\bar{B}$  (right)

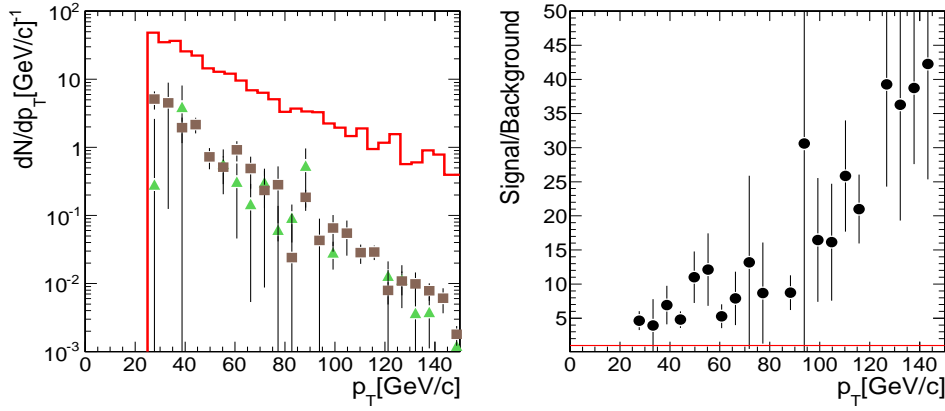


**Figure 5.** Left: The  $Z^0$ +jet and background yields in the range  $81 < M < 101 \text{ GeV}/c^2$  assuming  $L = 0.5 \text{ nb}^{-1}$ . The histogram shows the signal while the triangles and the squares are the  $D\bar{D}$  and  $B\bar{B}$  yields respectively. Right: The signal-to-background ratio. The errors reflect the background statistics only. The line indicates a signal-to-background ratio of unity.

decays. The circles are results with no kinematic cuts on either the individual muons or the muon pairs. The triangles include the detector cuts on single muons as well as a pair cut of  $p_T^{\mu\mu} > 25 \text{ GeV}/c$ .

Figure 4 shows the dimuon mass distributions for  $D\bar{D}$  (left) and  $B\bar{B}$  (right) decays. The filled circles correspond to no kinematic cuts on either the single muons or the pair. The remaining results include single muon detector cuts along with  $p_T^{\mu\mu} > 25, 40$  and  $50 \text{ GeV}/c$ .

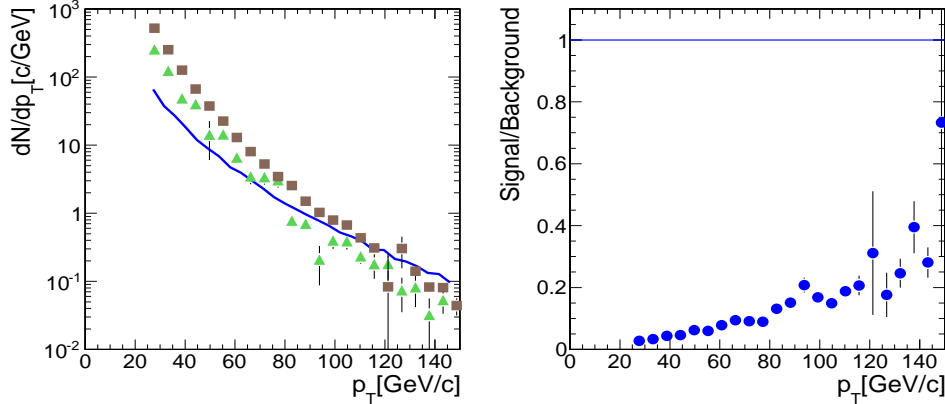


**Figure 6.** Left: The annual  $\gamma^*$ +jet signal and heavy flavor background dimuon yields in the mass range  $12 < M < 81 \text{ GeV}/c^2$  for  $L = 0.5 \text{ nb}^{-1}$ . The line is the signal, the triangles and the squares are the  $D\bar{D}$  and  $B\bar{B}$  yields respectively. Right: The signal-to-background ratio. The errors reflect the background statistics only.

**Signal and Background Rates.** We now compare the background rates to the signal dimuon rates from  $Z^0/\gamma^*$  decays. The left-hand side of Fig. 5 shows the rates as a function of  $p_T^{\mu\mu}$  in the dimuon invariant mass range  $81 < M < 101 \text{ GeV}/c^2$ , the  $Z^0$  mass

region. The signal-to-background ratio is greater than unity for all  $p_T^{\mu\mu}$  and increases with  $p_T^{\mu\mu}$ , as shown on the right-hand side of Fig. 5.

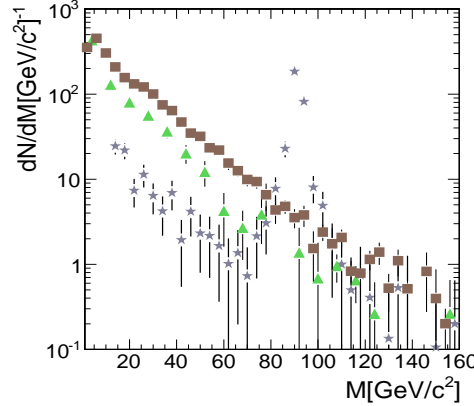


**Figure 7.** The dimuon invariant mass distribution for  $Z^0/\gamma^*$  and  $D\bar{D}/B\bar{B}$  decays assuming  $L = 0.5 \text{ nb}^{-1}$ . The stars are the signal, the triangles and the squares are the  $D\bar{D}$  and  $B\bar{B}$  yields respectively.

The same results are shown in the invariant mass region from above the  $\Upsilon$  family to below the  $Z^0$  peak,  $12 < M < 81 \text{ GeV}/c^2$ , in Fig. 6. In this case, the signal dimuons from  $\gamma^*$  production are overwhelmed by the heavy meson decays over the entire  $p_T^{\mu\mu}$  range shown.

In both Figs. 5 and 6, the error bars on the heavy flavor decay backgrounds are statistical only. They reflect the steeper fall of the  $D$  meson spectra relative to  $B$  meson spectra and hence the poorer  $D$  statistics in the large invariant mass region.

Figure 7 shows the invariant mass distributions for the  $Z^0/\gamma^*$  signal and the heavy flavor decay background. Below the  $Z^0$  peak, the mass distribution is dominated by the heavy flavor background while the  $Z^0$  peak is well above the background. Thus in a one month heavy-ion run at  $L = 0.5 \text{ nb}^{-1}$ , it is possible to extract a  $Z^0$ -jet signal free from contamination. Additional cuts will have to be applied in order to increase the signal-to-background ratio in the  $\gamma^*$ -jet channel. Several possible cuts are investigated in Section 5.

We now briefly discuss the theoretical uncertainties in the  $Q\bar{Q}$  background. Generally speaking, the total cross section for heavy quark production is affected by uncertainties on the order of 50% or larger. The charm uncertainty is larger than for bottom due to the smaller mass and consequently smaller renormalization and factorization scales. The choice of PDFs is also a source of uncertainty [24]. However, the largest uncertainties are concentrated at low transverse momentum,  $p_T < 5 \text{ GeV}/c$ . Since our studies focus on the high- $Q^2$  region, the uncertainty in the results presented here is 10-20 %. Thus, even if we assume the upper limit of the uncertainty to be correct, the  $Z^0$ -jet signal will still stand out well above the heavy flavor background.

## 4.2. Dijets

Dijets can contribute to the dilepton background in two ways. Very energetic light hadrons (pions, kaons and protons) that escape the hadron absorber can be identified as muons in the muon detectors. These hadrons are called *punch-through* hadrons. In-flight decays of pions,  $B(\pi \rightarrow \mu\nu) = 99\%$ , and kaons,  $B(K \rightarrow \mu X) = 63\%$  can contribute to the dilepton background.

We assume that punch-through hadrons are most important at high  $p_T^{\mu\mu}$  while the dimuons from light hadron decays mainly contribute at low  $p_T^{\mu\mu}$ . Since we consider the case  $p_T^{\mu\mu} > 25 \text{ GeV}/c$ , it is likely that punch-throughs are the main dijet background.

This kind of background level is detector specific and a detailed estimate can only be determined after a full muon reconstruction analysis. Since we do not include detector simulations here, we only note that the punch-through background can be accounted for by performing a like-sign subtraction ( $\mu^+\mu^+, \mu^-\mu^-$ ).

## 5. Background Rejection

### 5.1. Rejecting heavy-flavor decays by distance of closest approach

We investigated a distance of closest approach (DCA) cut on the single muons and muon pairs to reject the heavy flavor background. This rejection method is possible because the  $\gamma^*$  and  $Z^0$  signal decays to dimuons with negligible decay lengths while the heavy flavor background comes from decays with measurable decay lengths. We present the results obtained with a DCA cut between the primary vertex and each muon trajectory (two separate “point-to-line” DCA cuts OR’ed together). We also considered, in addition to the point-to-line DCA cuts, one between the two muon trajectories (one “line-to-line” DCA cut). This additional line-to-line DCA cut improves the results presented below by a few percent. The basic formulae for both types of DCA cuts are presented in Appendix B.

**5.1.1. PYTHIA simulation** The PYTHIA event generator is used to generate  $pp$  collisions at  $\sqrt{s_{NN}} = 5.5 \text{ TeV}$ , keeping only  $Q\bar{Q}$  events which subsequently decay to dileptons. Two data samples were analyzed: one with 50 M collisions with  $\hat{p}_T^{\text{hard}} > 15 \text{ GeV}/c$ , the “triggered” set and another with 100 M collisions with  $\hat{p}_T^{\text{hard}} > 2 \text{ GeV}/c$ , the “minimum-bias” set. This method significantly decreased the simulation time for producing a high-momentum heavy-flavor dimuon data sample. A comparison of the distributions of decay parameters (decay vertex position, decay angle and DCA) from the two sets was made in order to check that the trigger bias has no effect on the decay kinematics.

We use the lepton momentum rather than the heavy-flavor meson momentum because the leptons are the experimental observable. Figure 8 shows the fraction of the meson momentum transferred to the decay lepton. On average, the decay muon retains 40-60% of the parent hadron momentum.

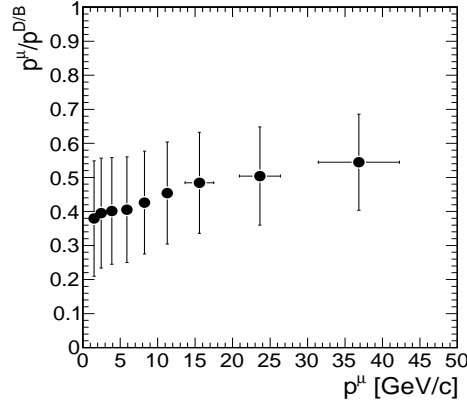


**Figure 8.** The fraction of heavy flavor momentum transferred to the decay lepton as a function of the lepton momentum.

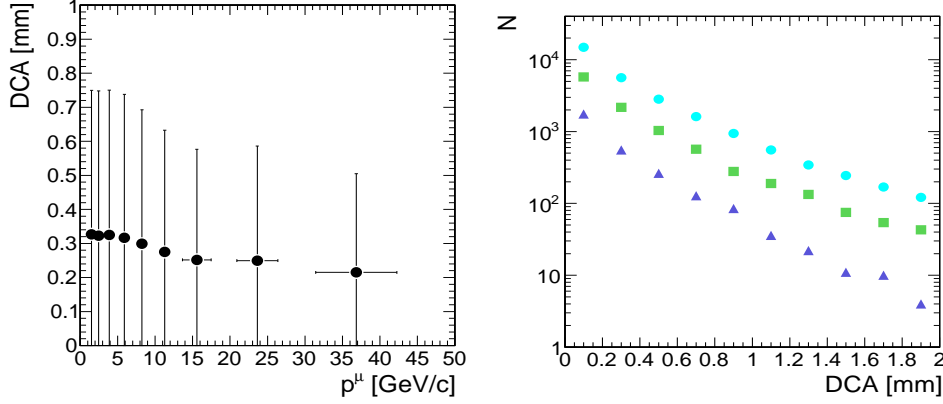


**Figure 9.** Left: The DCA profile as a function of lepton momentum. The central values are the mean and the errors represent the RMS variance. Right: Examples of DCA distributions used to extract the mean and RMS of the DCA profile on the left-hand side. The shapes correspond to three  $p^\mu$  intervals:  $3 < p^\mu < 5$  GeV/c (circles),  $10 < p^\mu < 13$  GeV/c (squares), and  $20 < p^\mu < 30$  GeV/c (triangles).

*5.1.2. Two point-to-line DCA cuts* Since, at the generator level, there is no magnetic field (charged particle trajectories are straight lines) and the collision primary vertex is always at the origin of the laboratory reference frame, the DCA geometry becomes very simple. The resulting analytic formulas are described in detail in Appendix B. The left-hand side of Fig. 9 shows a profile plot (the points are the mean values while error bars are RMS values of the distributions on the right-hand-side of Fig. 9) of the DCA vector magnitude as a function of the lepton momentum.

The magnitude of the DCA vector is a convolution of the decay angle with the length of the secondary decay vertex. Hence, in order to understand the momentum dependence of the DCA, we plot the profile of the momentum dependence of these two quantities on the left-hand side of Fig. 10. The right-hand side of Fig. 10 shows examples of distributions from which the profiles on the left-hand side were extracted for

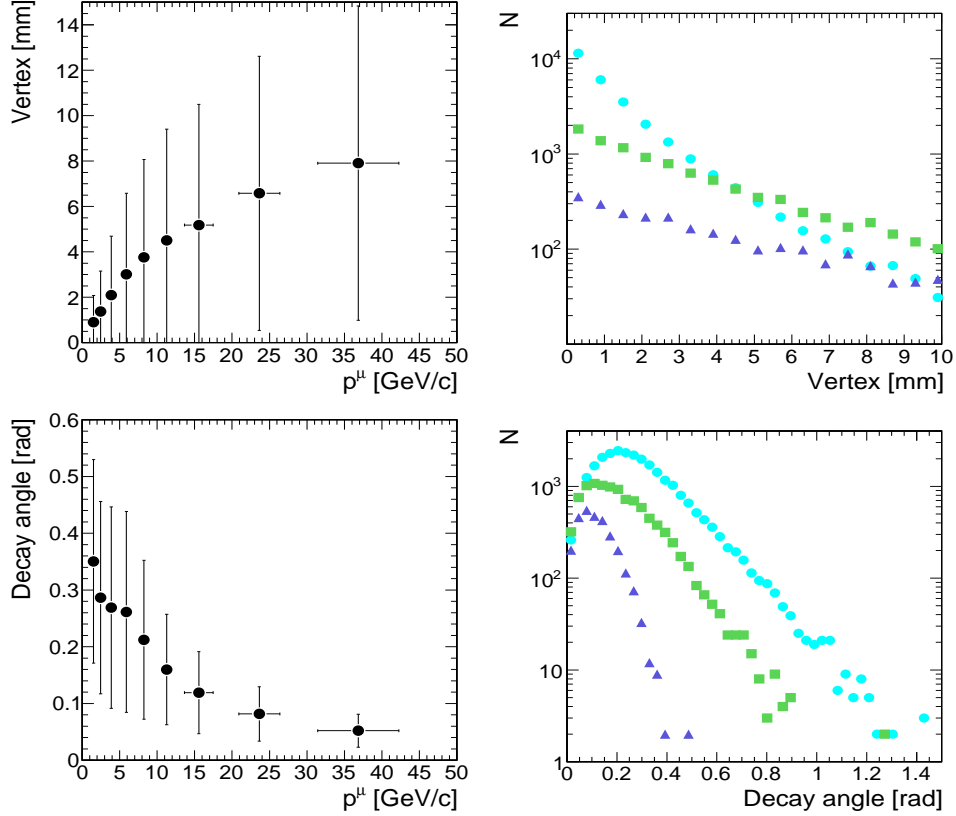


**Figure 10.** The secondary vertex position (top) and decay angle (bottom) as a function of lepton momentum. Left: The secondary vertex position and decay angle as a function of lepton momentum. The central values are the mean and the errors represent the RMS variance. Right: Examples of DCA distributions used to extract the mean and RMS shown on the left-hand side. The symbols correspond to  $p^\mu$  intervals:  $3 < p^\mu < 5$  GeV/c (circles),  $10 < p^\mu < 13$  GeV/c (squares), and  $20 < p^\mu < 30$  GeV/c (triangles).

three different  $p^\mu$  intervals, chosen to sample the low, intermediate and high- $p_T$  muon kinematic regions.

The decay is further from the primary vertex at higher lepton momenta while the decay angle decreases. The two effects approximately cancel each other but the decreasing decay angle appears to become dominant at very high lepton momenta, as shown by the slowly decreasing DCA on the left-hand side of Fig. 9.

Finally, we estimate the dilepton rejection factor for heavy flavor decays using a DCA cut typical for the CMS silicon vertex tracker. The DCA resolution in the heavy-ion environment was estimated [16] to be  $\sigma_{r\phi} \approx 20 \mu\text{m}$  in the transverse plane and  $\sigma_{rz} \approx 50 \mu\text{m}$  in the longitudinal plane. Figure 11 shows the rejection factor with a  $3\sigma$  DCA cut, corresponding to  $\text{DCA}(r\phi) > 60 \mu\text{m}$  or  $\text{DCA}(rz) > 150 \mu\text{m}$ . Note that, in Fig. 11, the vertical error bars are no longer rms values but statistical errors. Hence, a rejection factor of about 5 can be obtained by two simple point-to-line DCA cuts between each lepton trajectory and the primary vertex, OR'ed together (*i.e.* requiring

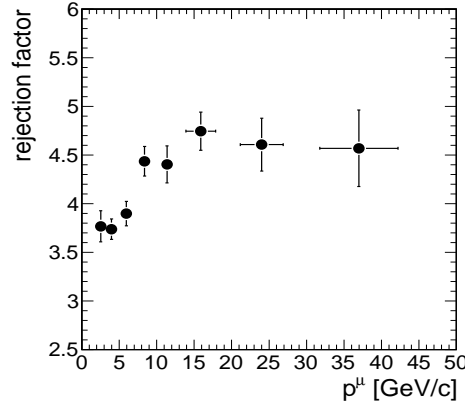


**Figure 11.** The DCA rejection factor in the CMS silicon vertex tracker with a  $3\sigma$  DCA cut. The vertical error bars are statistical while the horizontal error bars represent the RMS of the momentum.

at least one of the DCAs to be larger than a  $3\sigma$  cut). An additional line-to-line DCA increases the rejection factor by less than 5%.

### 5.2. Rejecting heavy-flavor decays by dilepton kinematics

We also studied the  $Z^0/\gamma^*$  dilepton kinematics relative to dileptons from heavy flavor decays. Because the signal is a two-body decay while the background includes fragmentation followed by three-body decays, we expect significant differences in the signal and background dilepton kinematics that could help disentangle the dimuon signal from its background.

The variables we chose are the dilepton opening angle,  $\Delta\Phi = \Phi_{l_1} - \Phi_{l_2}$ , the pseudorapidity difference,  $\Delta\eta = \eta_{l_1} - \eta_{l_2}$ , and momentum asymmetry,  $\xi = |p_{l_1} - p_{l_2}| / (p_{l_1} + p_{l_2})$ . We sampled three different dimuon,  $p_T^{\mu\mu}$ , intervals,  $25 < p_T^{\mu\mu} < 40$  GeV/c,  $40 < p_T^{\mu\mu} < 60$  GeV/c, and  $p_T^{\mu\mu} > 60$  GeV/c for the  $Z^0$  mass region,  $81 < M < 101$  GeV/ $c^2$ , and the continuum,  $12 < M < 70$  GeV/ $c^2$ . We did not choose higher  $p_T^{\mu\mu}$  intervals because of the limited statistics available at high momentum.

Figure 12 shows the normalized  $\Delta\Phi$  distribution for  $25 < p_T^{\mu\mu} < 40$  GeV/c from  $Z^0$  (left) and  $\gamma^*$  (right) decays, together with the corresponding backgrounds. Since the characteristics of these distributions were found to be similar for the other two  $p_T$  intervals studied, we chose to show only the case with the highest signal yield. While the  $Z^0$  signal and background dimuons have relatively the same features, there is a more visible difference in the case of  $\gamma^*$  dimuons. In both cases, we estimated the effect of a  $\Delta\Phi$  cut on the signal and background distributions.

We extract the *fractional yields* for each distribution by integrating the distributions above (for  $Z^0$ ) or below (for  $\gamma^*$ ) a specified  $\Delta\Phi$  cut. The results are presented in Fig. 13. The left-hand side gives the fractional yields of the  $Z^0$  decays and the heavy-flavor backgrounds. There is no significant difference between the signal and background



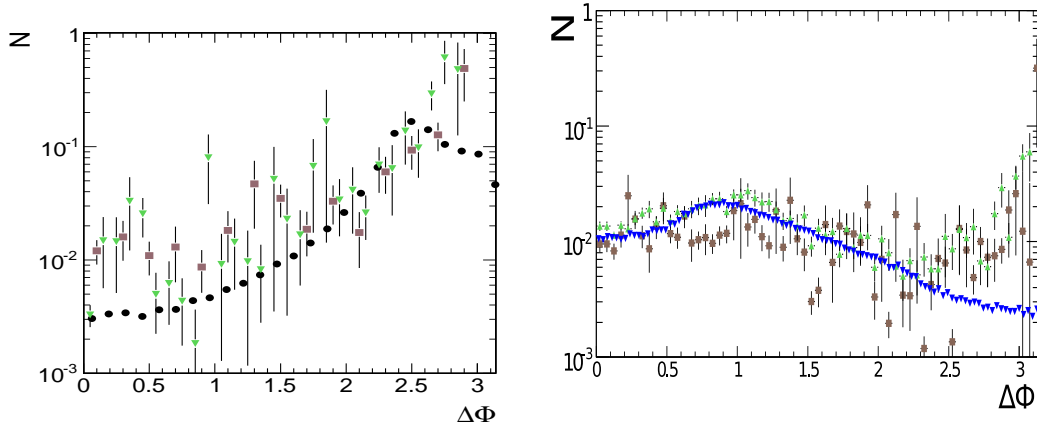


**Figure 12.** The normalized  $\Delta\Phi$  distributions for  $Z^0$  ( $81 < M < 101 \text{ GeV}/c^2$ ) (left) and  $\gamma^*$  ( $12 < M < 70 \text{ GeV}/c^2$ ) (right) for  $25 < p_T^{\mu\mu} < 40 \text{ GeV}/c$ . The circles are from  $Z^0$ , the inverse triangles from  $\gamma^*$ , the triangles from  $D\bar{D}$  decays and the squares from  $B\bar{B}$  decays.

dileptons for any  $\Delta\Phi$  cut. Thus, a kinematic cut based on  $\Delta\Phi$  angle between the two muons, cannot improve the already good signal-to-background ratio for  $Z^0$ +jet signal, see Fig. 5. The right-hand side of Fig. 13 shows the fractional yields for  $\gamma^* \rightarrow \mu^+\mu^-$  and the corresponding backgrounds. With  $\Delta\Phi \leq 2.5 \text{ rad}$ , we preserve  $\approx 95\%$  of the  $\gamma^*$  signal while eliminating  $\approx 25\%$  of the  $D\bar{D}$  and  $\approx 45\%$  of the  $B\bar{B}$  background, improving the low  $S/B$  ratio in Fig. 6.

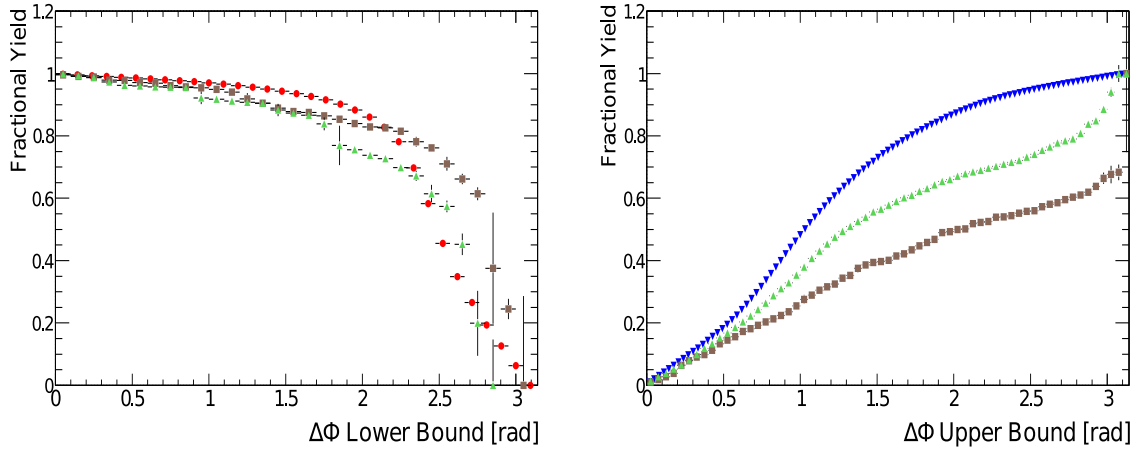


**Figure 13.** The effect of a lower bound on  $\Delta\Phi$  ( $Z^0$ ,  $81 < M < 101 \text{ GeV}/c^2$ , left) and an upper bound on  $\Delta\Phi$  ( $\gamma^*$ ,  $12 < M < 70 \text{ GeV}/c^2$ , right) for  $25 < p_T^{\mu\mu} < 40 \text{ GeV}/c$ . The circles are from  $Z^0$ , the inverse triangles from  $\gamma^*$ , the triangles from  $D\bar{D}$  decays and the squares from  $B\bar{B}$  decays.

### 5.3. Isolating signal employing shape differences between correlation functions

In addition to cuts based on differences between the signal and background decay kinematics, the two-body angular correlation method itself will help isolate the signal from residual backgrounds.

The statistical analysis of the angular correlation between all dimuons and hadrons in an event will produce a flat combinatorial distribution of background relative to the signal. Any deviation of the uniform background correlation shape can be identified by same-sign lepton pair correlations relative to opposite-sign or mixed-flavor ( $e\mu$ ) dilepton correlations. Moreover, the combination of a mixed-flavor and a same-sign dilepton analysis can isolate the dimuon signal in the mass region below the  $Z^0$  since the  $\gamma^*$  decays only in opposite-sign, same-flavor dileptons.

## 6. Conclusions

We have presented a case study for measuring dilepton-tagged jets via angular correlations at the LHC. The signal rates,  $Z^0/\gamma^*(\rightarrow \mu\mu) + \text{jet}$  were computed with the PYTHIA event generator while the main dilepton background source, semileptonic decays of heavy mesons,  $D\bar{D}/B\bar{B} \rightarrow \mu\mu$ , was calculated at NLO with HVQMR.

Detailed kinematical studies of both signal (the dimuon tag and the associated away jet) and background were performed in order to study the feasibility of the measurement at the LHC in Pb+Pb collisions. Several cuts were discussed that can increase the signal-to-background ratio,  $S/B$ .

Below the  $Z^0$  mass peak, the dimuon mass distribution is dominated by the heavy-flavor background. The kinematic analysis of the dimuons from  $\gamma^*$  decays and from  $D\bar{D}/B\bar{B} \rightarrow \mu\mu$ , revealed no clear difference between the two dimuon sources. Hence, for the  $\gamma^*$ +jet signal other methods of background subtraction will have to be used. We thus estimate that a rejection factor of about 5 for heavy-flavor dimuons can be obtained by two simple DCA cuts between each lepton trajectory and the primary vertex, OR'ed together (*i.e.* requesting *at least one* of the DCAs to be larger than a  $3\sigma$  cut). However, this cut alone is not enough to overcome the  $S/B < 0.4$  for  $p_T^{\gamma^* \rightarrow \mu\mu} > 25 \text{ GeV}/c$ . A cut on the azimuthal opening angle between the leptons,  $\Delta\Phi$ , can improve the  $S/B$  ratio. In addition, a same-sign ( $\mu^+\mu^+, \mu^-\mu^-$ ) and/or a mixed-flavor lepton ( $e\mu$ ) analysis are two additional methods for disentangling the  $\gamma^* \rightarrow \mu\mu$  signal from the background.

For the  $Z^0$ +jet signal with  $p_T^{\mu\mu} > 25 \text{ GeV}/c$ ,  $S/B > 5$  in the kinematic region analyzed without any additional cuts imposed on the dimuon background. Thus it should be possible to extract a clean signal in a one month heavy-ion run at  $L = 0.5 \text{ nb}^{-1}$ . This will allow a complimentary low-momentum measurement of in-medium parton fragmentation distributions relative to the  $\gamma$ +jet analysis. Such a measurement is energetically possible for the first time in heavy-ion collisions at the LHC and opens new avenues for studying the properties of the QGP.

**Acknowledgements**

The authors thank Constantinos Loizides for assistance with the software infrastructure needed for this analysis. We also thank Carlos Lourenço for comments and suggestions. The work of R.V. was performed under the auspices of the U.S. Department of Energy by Lawrence Livermore National Laboratory under Contract DE-AC52-07NA27344 and was also supported in part by the National Science Foundation Grant NSF PHY-0555660.

## Appendix A. Contributions to the $\Delta\phi$ distributions

The PYTHIA event generator was used to simulate the various contributions to the  $\Delta\phi = \phi^{\text{trig}} - \phi^{\text{assoc}}$  distribution where the trigger dimuon comes from  $Z^0/\gamma^*$  decays and the associated particles come from the jet *right*?. In order to better understand the  $k_T$  contributions, we made several PYTHIA simulations with  $k_T^{\text{RMS}} = \langle k_T^2 \rangle^{1/2} = 0, 3$ , and  $5 \text{ GeV}/c$ . For each  $k_T$  setting we turned the initial and final-state radiation on and off to estimate the  $k_T$  contribution to the  $\Delta\phi$  distribution.

The  $\Delta\phi$  distribution has three main contributions:

$$\Delta\phi = \Delta\phi_0 + \Delta\phi_1 + \Delta\phi_2$$

where  $\Delta\phi_0$  is the contribution from the initial parton transverse momentum,  $k_T$ ;  $\Delta\phi_1$  is from the transverse momentum accrued during fragmentation,  $j_T$ ; and  $\Delta\phi_2$  is due to the multiple scattering (initial and final-state radiation) contribution.

Assuming that these three contributions are independent,

$$\sigma_{\Delta\phi}^2 = \sigma_{\Delta\phi_0}^2 + \sigma_{\Delta\phi_1}^2 + \sigma_{\Delta\phi_2}^2 .$$

We can further approximate  $\sigma_{\Delta\phi_0}$  by  $\Delta\phi_0 \approx k_T/p_T^{\text{trig}}$ . Thus

$$\sigma_{\Delta\phi_0} = \sqrt{\langle \Delta\phi_0^2 \rangle} \approx \left\langle \left( \frac{k_T}{p_T^{\text{trig}}} \right)^2 \right\rangle^{1/2} \approx \left( \frac{\langle k_T^2 \rangle}{\langle p_T^{\text{trig}2} \rangle} \right)^{1/2} \approx \frac{k_T^{\text{RMS}}}{\sqrt{\langle p_T^{\text{trig}2} \rangle}} = \frac{k_T^{\text{RMS}}}{\langle p_T^{\text{trig}} \rangle} .$$

Similarly it can be shown that the fragmentation contribution can be approximated by

$$\sigma_{\Delta\phi_1} = \sqrt{\langle \Delta\phi_1^2 \rangle} = \frac{j_T^{\text{RMS}}}{\langle p_T^{\text{trig}} \rangle} .$$

Though fragmentation cannot be turned off, its effect can be estimated. The values of  $\sigma_{\Delta\phi}$  for several different  $k_T$  settings with an average dilepton  $p_T$  of  $\langle p_T^{\text{trig}} \rangle = 25 \text{ GeV}/c$  are given in Table A1. The values of  $\sigma_{\Delta\phi_1}$  and the consequent  $j_T$  values determined from the PYTHIA  $\sigma_{\Delta\phi}$  with initial and final-state radiation turned off are used to calculate the contribution from initial and final-state radiation when these effects are included in the simulation.

**Table A1.** The contributions to  $\sigma_{\Delta\phi}$  for  $\langle p_T^{\text{trig}} \rangle = 25 \text{ GeV}/c$ .

PYTHIA Settings	$\sigma_{\Delta\phi}$	$\sigma_{\Delta\phi_0}$	$\sigma_{\Delta\phi_1}$	$\sigma_{\Delta\phi_2}$
$k_T^{\text{RMS}} = 0 \text{ GeV}/c$ , radiation = OFF	0.088	0	0.088	0
$k_T^{\text{RMS}} = 3 \text{ GeV}/c$ , radiation = OFF	0.158	0.115	0.108	0
$k_T^{\text{RMS}} = 5 \text{ GeV}/c$ , radiation = OFF	0.212	0.192	0.090	0
$k_T^{\text{RMS}} = 0 \text{ GeV}/c$ , radiation = ON	0.235	0	0.088	0.218
$k_T^{\text{RMS}} = 3 \text{ GeV}/c$ , radiation = ON	0.284	0.115	0.108	0.236
$k_T^{\text{RMS}} = 5 \text{ GeV}/c$ , radiation = ON	0.305	0.192	0.090	0.218

We summarize the effective contributions to  $\sigma_{\Delta\phi}$  in Fig. A1. The effect of initial and final-state radiation in PYTHIA is clearly the largest factor in broadening the  $\Delta\phi$

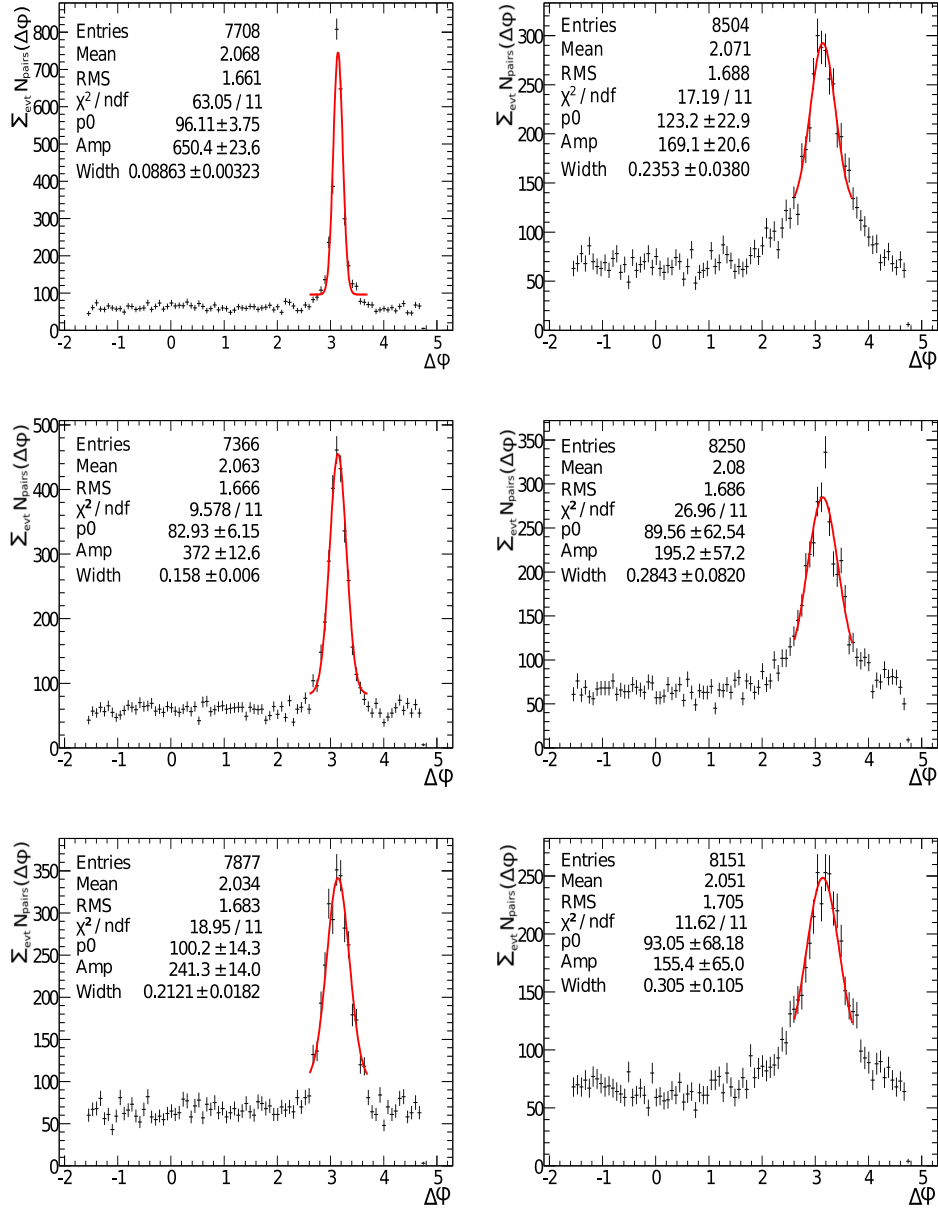


**Figure A1.** The effects of average intrinsic transverse momentum 0 (upper), 3 (middle) and  $k_T = 5$  GeV/c (bottom) on the  $\Delta\phi = \phi^{\text{trig}} - \phi^{\text{assoc}}$  distributions without (left-hand side) and with (right-hand side) initial and final-state radiation included.

distributions. For example, if  $\sigma_{\Delta\phi} \approx 0.3$  rad, the PYTHIA simulation suggests that  $\sigma_{\Delta\phi_0} \approx 0.19$  rad,  $\sigma_{\Delta\phi_1} \approx 0.1$  rad and  $\sigma_{\Delta\phi_2} \approx 0.22$  rad for  $\langle p_T^{\text{trig}} \rangle = 25$  GeV/c.

## Appendix B. Distance of Closest Approach Geometry

### Appendix B.1. The point-to-line DCA

The distance of closest approach (DCA) between a 3-dimensional point and a 3-dimensional line is a 2-dimensional geometry problem because a plane can always be found that contains the point and the line. Figure B1 shows that the DCA vector,  $\vec{d}$ , always belongs to the  $(\vec{r}, \vec{p})$  plane. Thus,

$$\vec{d} = \vec{r} + \alpha \vec{p} . \quad (\text{B.1})$$

Since by definition,  $\vec{d} \perp \vec{p}$ , we have  $\vec{d} \cdot \vec{p} = 0$ , giving

$$\alpha = -\frac{\vec{r} \cdot \vec{p}}{p^2} . \quad (\text{B.2})$$

Note that we have assumed the origin of the reference system is at  $(0, 0, 0)$ . We also assume straight line trajectories, *i.e.* no magnetic field.

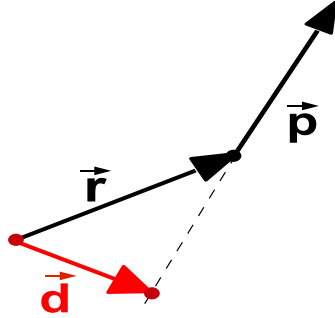


**Figure B1.** The point-to-line DCA geometry.

### Appendix B.2. The line-to-line DCA

The distance of closest approach geometry between two lines is more complex because two 3-dimensional (3D) lines are not coplanar. Figure B2 shows the basic geometry for this problem. A line in a plane  $s$ ,  $L(s)$ , can be specified either by a combination of two 3D points (*e.g.*  $P_0$  and  $P_1$ , with the position vectors  $\vec{r}_0$  and  $\vec{r}_1$  respectively) or a combination of one 3D point and one 3D vector (the same  $P_0$  point and  $\vec{p}$ , the 3D vector between  $P_0$  and  $P_1$ ). The line thus has the general form

$$L(s) = \vec{r}_0 + \alpha(\vec{r}_1 - \vec{r}_0) \equiv \vec{r}_0 + \alpha \vec{p} , \quad (\text{B.3})$$

where  $\alpha$  is a parameter. If we define two 3D lines, in two different planes, as

$$L_i(s_i) = \vec{r}_{0i} + \alpha_i \vec{p}_i, \quad i = 1, 2, \quad (\text{B.4})$$

the vector  $\vec{d}$  between two arbitrary points  $P_1$  and  $P_2$  on these two lines is

$$\vec{d} = \vec{d}_0 + \alpha_1 \vec{p}_1 - \alpha_2 \vec{p}_2 \quad (\text{B.5})$$

where  $\vec{d}_0 \equiv \vec{r}_{01} - \vec{r}_{02}$ .

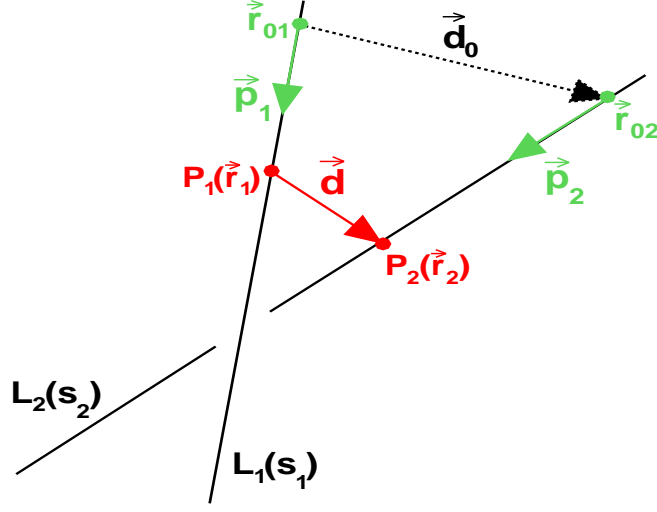


**Figure B2.** The line-to-line DCA geometry.

To find the DCA vector, we need to find the values of  $\alpha_1$  and  $\alpha_2$  that minimize  $|\vec{d}|$ . This is straightforward because  $|\vec{d}|$  is a minimum when it is orthogonal to both lines,  $\vec{p}_1 \cdot \vec{d} \equiv 0$  and  $\vec{p}_2 \cdot \vec{d} \equiv 0$ . Hence,

$$\vec{p}_1 \cdot (\vec{d}_0 + \alpha_1 \vec{p}_1 - \alpha_2 \vec{p}_2) = 0, \quad (\text{B.6})$$

$$\vec{p}_2 \cdot (\vec{d}_0 + \alpha_1 \vec{p}_1 - \alpha_2 \vec{p}_2) = 0. \quad (\text{B.7})$$

If we let  $\beta \equiv \vec{p}_1 \cdot \vec{p}_2$ , this can be simplified to

$$\vec{d}_0 \cdot \vec{p}_1 + p_1^2 \alpha_1 - \beta \alpha_2 = 0, \quad (\text{B.8})$$

$$\vec{d}_0 \cdot \vec{p}_2 + \beta \alpha_1 - p_2^2 \alpha_2 = 0. \quad (\text{B.9})$$

The DCA solution vector is

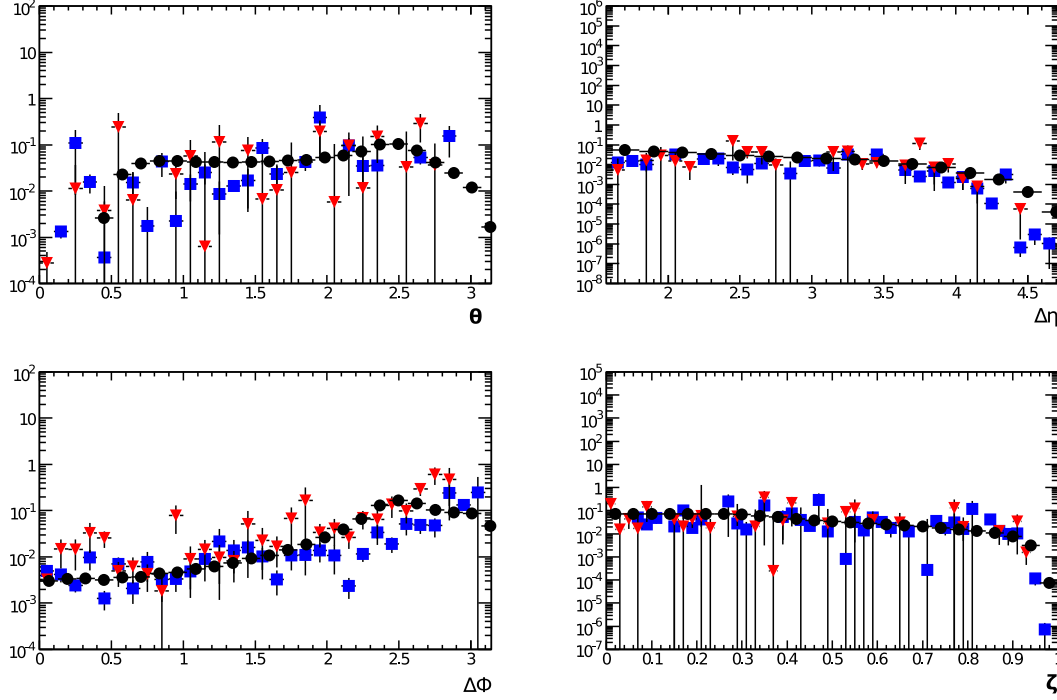
$$\vec{d} = (\vec{r}_{01} + \alpha_1 \vec{p}_1) - (\vec{r}_{02} + \alpha_2 \vec{p}_2) \quad (\text{B.10})$$

where  $\alpha_1$  and  $\alpha_2$  are

$$\alpha_1 = - \frac{p_2^2 \vec{p}_1 - \beta \vec{p}_2}{p_1^2 p_2^2 - \beta^2} \cdot (\vec{r}_{01} - \vec{r}_{02}), \quad (\text{B.11})$$

$$\alpha_2 = + \frac{p_1^2 \vec{p}_2 - \beta \vec{p}_1}{p_1^2 p_2^2 - \beta^2} \cdot (\vec{r}_{01} - \vec{r}_{02}). \quad (\text{B.12})$$

The only validity condition for this solution is that the two lines cannot be parallel or, equivalently, that  $\beta \neq p_1 p_2$ .

Appendix C.  $Z^0/\gamma^* \rightarrow \mu^+\mu^-$  decay kinematics

**Figure C1.** The normalized  $Z^0$  (circles),  $D\bar{D}$  (triangles), and  $B\bar{B}$  (squares) distributions as functions of the opening angle  $\theta$  (upper left),  $\Delta\eta$  (upper right),  $\Delta\Phi$  (lower left), and momentum asymmetry  $\zeta$  (lower right) for  $25 < p_T^{\mu\mu} < 40 \text{ GeV}/c$  and  $81 < M < 101 \text{ GeV}/c^2$ .

To simulate the  $Z^0/\gamma^*$  signal, a **ROOT** macro was created that calculates the 2-body decay of a particle at rest using relativistic kinematics. The macro can be adjusted for the desired particle masses and can generate an infinite number of decays. Using this “particle gun” we generated  $\gamma^*$  in the range  $12 < M < 70 \text{ GeV}/c^2$  and  $Z^0$  in the range  $81 < M < 101 \text{ GeV}/c^2$  ( $m_{Z^0} = 91.16 \text{ GeV}/c^2$ ), with uniform  $p_T$ ,  $\phi$  and  $\eta$  distributions. The  $Z^0/\gamma^*$  were boosted to their rest frame for decay into  $\mu^+\mu^-$  pairs. The muons were boosted back afterwards and the single muons were subjected to two cuts,  $|\eta^\mu| < 2.4$  and  $p_T^\mu > 3.5 \text{ GeV}/c$ , to simulate the CMS and ATLAS detector acceptances. The heavy flavor background is generated using the **HVQMNR** code in the same mass ranges as the  $Z^0/\gamma^*$  signals.

The following kinematic variables of the decay are studied: the dimuon opening angle (lab frame angle between the two muons),  $\theta$ ; the azimuthal angle difference between the two muons (transverse projection of the opening angle),  $\Delta\Phi = \Phi_{\mu_1} - \Phi_{\mu_2}$ ; the pseudorapidity difference between the muons (longitudinal projection of the opening angle),  $\Delta\eta = \eta_{\mu_1} - \eta_{\mu_2}$ ; and the dimuon momentum asymmetry,  $\zeta = |p_{\mu_1} - p_{\mu_2}| / (p_{\mu_1} + p_{\mu_2})$ . To examine the muon dependence of our chosen variables, we performed the analysis in three dimuon  $p_T$  intervals:  $25 < p_T^{\mu\mu} < 40$ ,  $40 < p_T^{\mu\mu} < 60$ , and



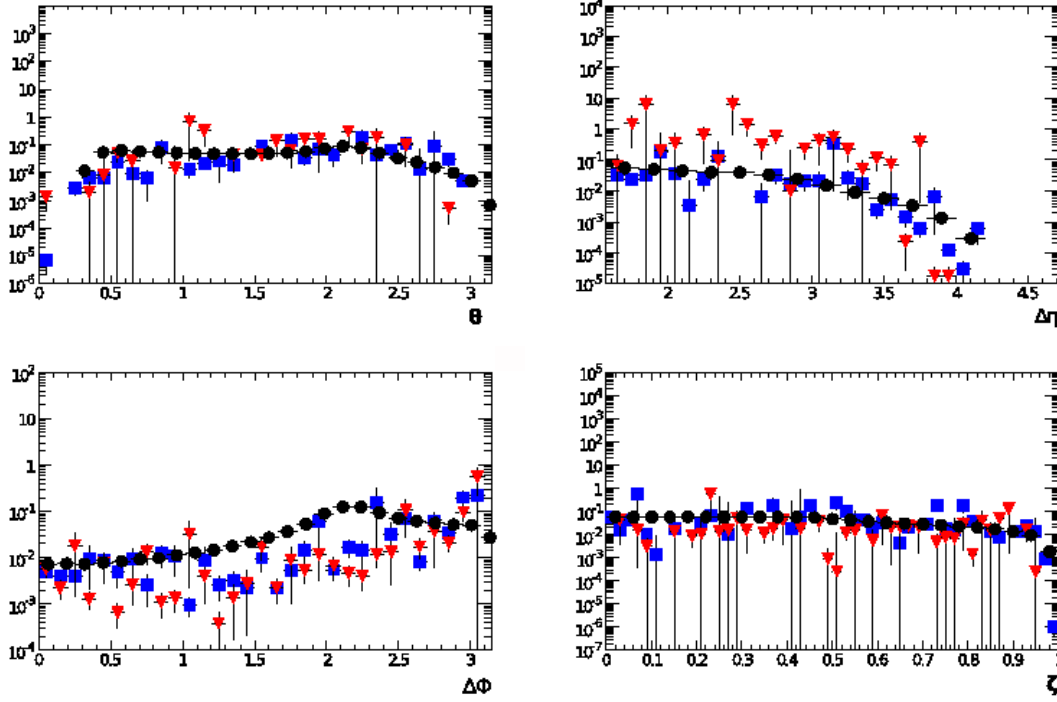


**Figure C2.** The normalized  $Z^0$  (circles),  $D\overline{D}$  (triangles), and  $B\overline{B}$  (squares) distributions as functions of the opening angle  $\theta$  (upper left),  $\Delta\eta$  (upper right),  $\Delta\Phi$  (lower left), and momentum asymmetry  $\zeta$  (lower right) for  $40 < p_T^{\mu\mu} < 60 \text{ GeV}/c$  and  $81 < M < 101 \text{ GeV}/c^2$ .

$p_T^{\mu\mu} > 60 \text{ GeV}/c$ . We did not choose higher  $p_T^{\mu\mu}$  intervals because of the limited statistics available at high momentum.

Figures C1-C3 show the momentum dependence of the dimuon distributions in the  $Z^0$  mass range, as a function of each of the kinematic variables. Figures C4-C6 show the same distributions in the  $\gamma^*$  mass range. The  $D\overline{D}$  and  $B\overline{B}$  backgrounds are also shown in the same mass regions as the signal. No significant differences are found between the signal and background dimuons for any of the kinematic variables studied.

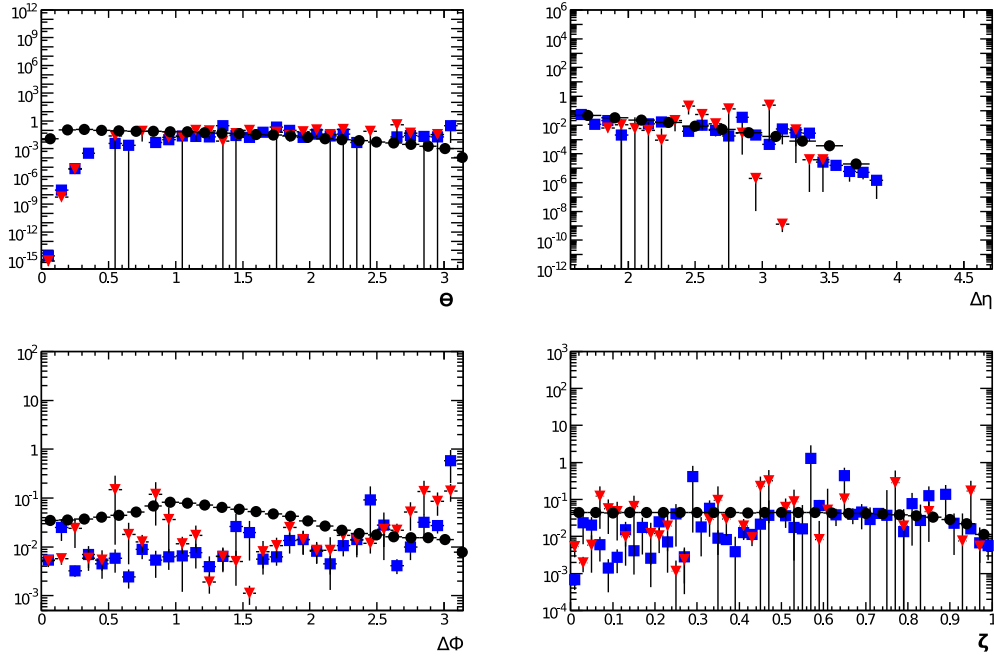


**Figure C3.** The normalized  $Z^0$  (circles),  $D\bar{D}$  (triangles), and  $B\bar{B}$  (squares) distributions as functions of the opening angle  $\theta$  (upper left),  $\Delta\eta$  (upper right),  $\Delta\Phi$  (lower left), and momentum asymmetry  $\zeta$  (lower right) for  $p_T^{\mu\mu} > 60 \text{ GeV}/c$  and  $81 < M < 101 \text{ GeV}/c^2$ .

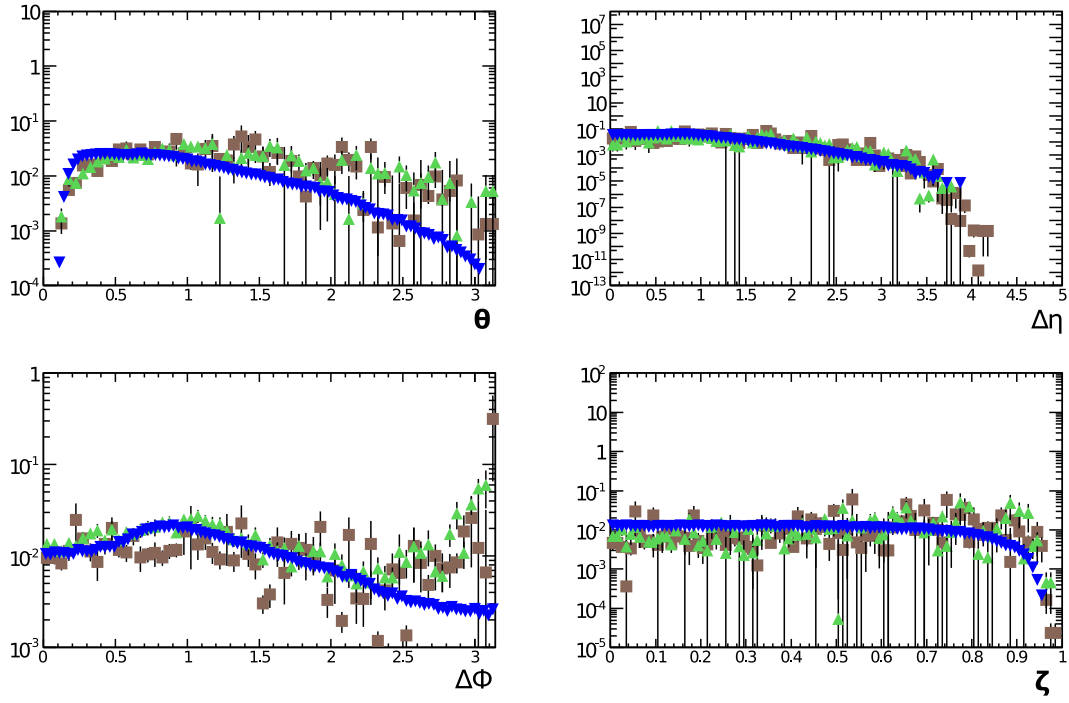


**Figure C4.** The normalized  $\gamma^*$  (triangles down),  $D\bar{D}$  (triangles up), and  $B\bar{B}$  (squares) distributions as functions of the opening angle  $\theta$  (upper left),  $\Delta\eta$  (upper right),  $\Delta\phi$  (lower left), and momentum asymmetry  $\zeta$  (lower right) for  $25 < p_T^{\mu\mu} < 40 \text{ GeV}/c$  and  $12 < M < 70 \text{ GeV}/c^2$ .

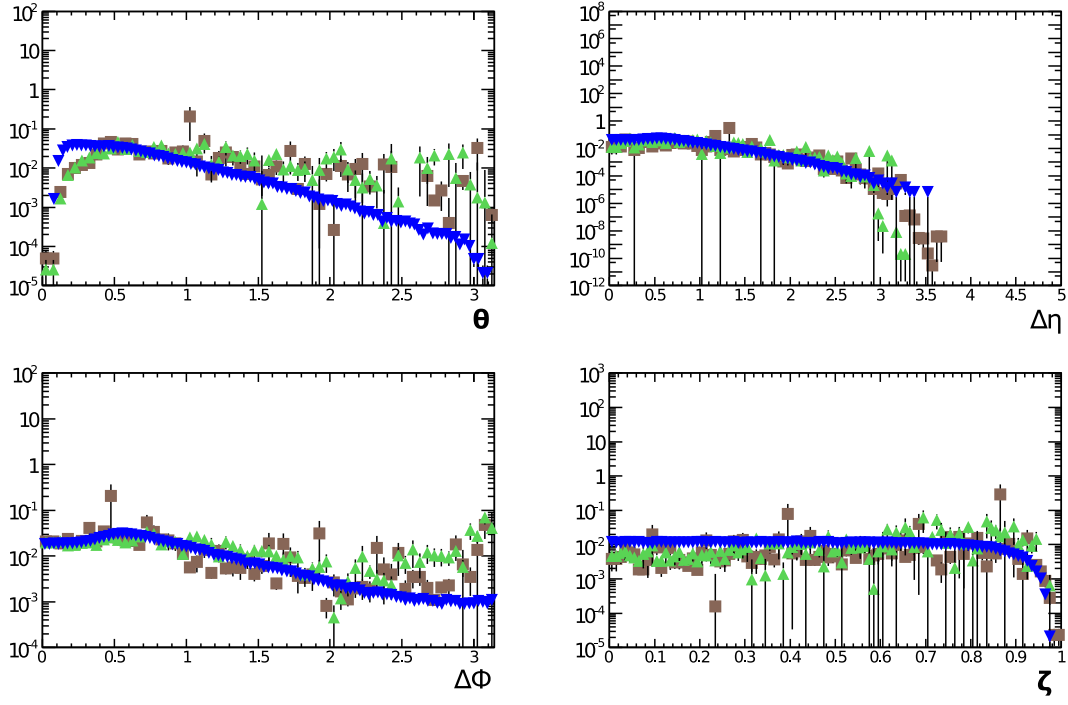


**Figure C5.** The normalized  $\gamma^*$  (triangles down),  $D\bar{D}$  (triangles up), and  $B\bar{B}$  (squares) distributions as functions of the opening angle  $\theta$  (upper left),  $\Delta\eta$  (upper right),  $\Delta\phi$  (lower left), and momentum asymmetry  $\zeta$  (lower right) for  $40 < p_T^{\mu\mu} < 60 \text{ GeV}/c$  and  $12 < M < 70 \text{ GeV}/c^2$ .

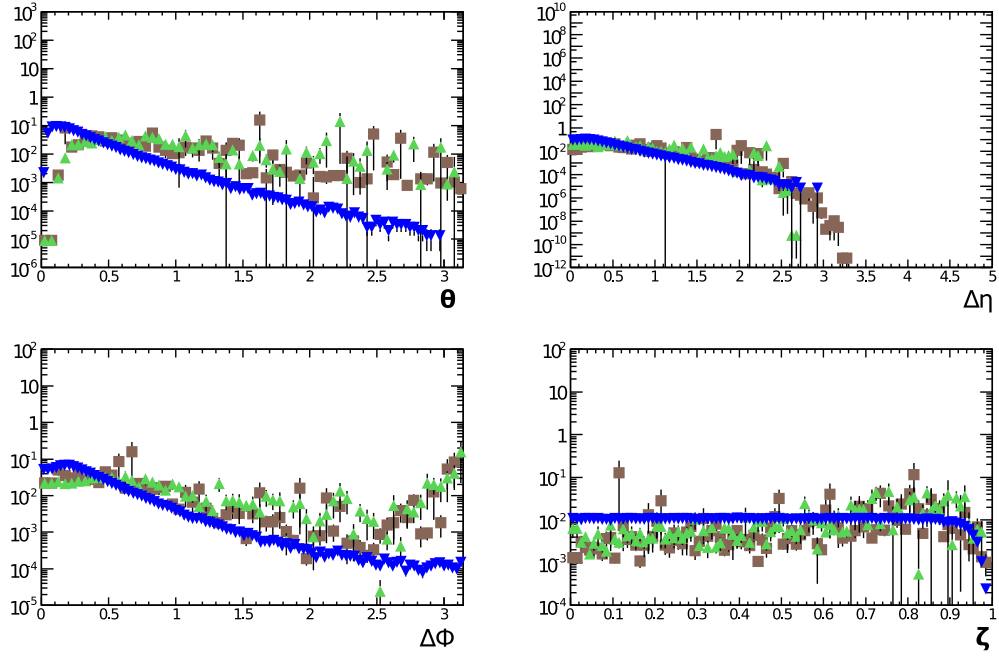


**Figure C6.** The normalized  $\gamma^*$  (triangles down),  $D\bar{D}$  (triangles up), and  $B\bar{B}$  (squares) distributions as functions of the opening angle  $\theta$  (upper left),  $\Delta\eta$  (upper right),  $\Delta\phi$  (lower left), and momentum asymmetry  $\zeta$  (lower right) for  $p_T^{\mu\mu} > 60 \text{ GeV}/c$  and  $12 < M < 70 \text{ GeV}/c^2$ .

- [1] I. Arsene *et al.* [BRAHMS Collaboration] 2005 *Nucl. Phys. A* **757** 1.  
 B. B. Back *et al.* [PHOBOS Collaboration] 2005 *Nucl. Phys. A* **757** 28.  
 J. Adams *et al.* [STAR Collaboration] 2005 *Nucl. Phys. A* **757** 102.  
 K. Adcox *et al.* [PHENIX Collaboration] 2005 *Nucl. Phys. A* **757** 184.
- [2] C. Adler *et al.* [STAR Collaboration] 2003 *Phys. Rev. Lett.* **90** 082302.
- [3] J. Adams *et al.* [STAR Collaboration] 2005 *Phys. Rev. Lett.* **95** 152301.
- [4] M. Gyulassy *et al.* 2000 *Phys. Rev. Lett.* **85** 5535.
- [5] V. Kartvelishvili, R. Kvatadze, and R. Shanidze 1995 *Phys. Lett. B* **356** 589.
- [6] I. P. Lokhtin, A. V. Sherstnev, and A. M. Snigirev 2004 *Phys. Lett. B* **599** 260.
- [7] S. Salur 2009 *Preprint* nucl-ex/09074536.
- [8] G. Arnison *et al.* 1983 *Phys. Rev. D* **123** 115.
- [9] X.-N. Wang, Z. Huang, and I. Sarcevic 1996 *Phys. Rev. Lett.* **77** 231.
- [10] X.-N. Wang and Z. Huang 1997 *Phys. Rev. C* **55** 3047.
- [11] P. Aurenche *et al.* 1999 *Eur. Phys. J. C* **9** 107.
- [12] Y. Chen *et al.* [CMS Collaboraiton] 2009 *Eur. Phys. J. C* **61** 649.
- [13] M. D. Baker *et al.* [ATLAS Collaboration] 2009 *Nucl. Phys.* A830 499c.
- [14] T. Sjöstrand *et al.* 2003 *Preprint* hep-ph/0308153.
- [15] L. Apanasevich *et al.* 1999 *Phys. Rev. D* **59** 074007.
- [16] C. Roland *et al.* [CMS Collaboration] 2006 *Nucl. Instrum. Meth. A* **566** 123.
- [17] J. Dolejsi *et al.* [ATLAS Collaboration] 2009 *Nucl. Phys. A* **830** 89C.
- [18] M. Bedjidian *et al.* 2003 *Preprint* hep-ph/0311048.
- [19] C. Mironov, R. Vogt, and G. J. Kunde 2009 *Eur. Phys. J. C* **61** 893.
- [20] M. Mangano, P. Nason, and G. Ridolfi 1992 *Nucl. Phys. B* **373** 295.
- [21] C. Peterson *et al.* 1983 *Phys. Rev. D* **27** 105.
- [22] J. Pumplin *et al.* 2002 *JHEP* **0207** 012.
- [23] M. Cacciari, P. Nason, and R. Vogt 2005 *Phys. Rev. Lett.* **95** 122001.
- [24] R. Vogt *Eur. Phys. J. C* **61** 893.  
 M. Cacciari <http://cacciari.web.cern.ch/cacciari/talks/lbl.pdf>